Mathematics

https://www.aimspress.com/journal/Math

AIMS Mathematics, 11(8): 24353–24378.
DOI:10.3934/math.2026983
Received: 20 June 2026
Revised: 21 July 2026
Accepted: 24 July 2026
Published: 10 August 2026

Research article

Existence, stability, and synchronization of fractional spatiotemporal chaotic systems with purely integral boundary conditions

Abdellah Menasri[1,2] **and Ahcene Merad**[2,*]

[1] Higher National School of Forests, Khenchela, Algeria

[2] System Dynamics and Control Laboratory, Department of Mathematics and Informatics, Oum El Bouaghi University, Algeria

* **Correspondence:** Email: ahcene.merad@univ-oeb.dz.

Abstract: We establish a rigorous operator framework for drive–response time-fractional reaction–diffusion equations under two integral moment constraints. The constrained state and energy spaces are explicitly defined, and the diffusion operator is constructed by a coercive closed form. We prove density of its domain, compactness of its resolvent, identification of its square-root space, and characterization of its strong domain; an explicit trace-surjectivity argument distinguishes the essential moment constraints from the natural zero-flux relations selected by the form. Nonhomogeneous moments are treated through an explicit lifting. For nonlinearities depending on the state and its spatial derivative, fractional resolvent estimates yield unique global mild solutions in the energy space without treating the unbounded elliptic operator as bounded or restarting the Caputo problem. A spectral Galerkin approximation lemma justifies the passage from the finite-dimensional energy inequality to the mild solution. Then, the synchronization error satisfies a computable Mittag–Leffler estimate in which the gradient mismatch is explicitly absorbed by diffusion. A moment-preserving spectral–L1 discretization verifies the analytical gain threshold, moment conservation, fractional orders below 0.9, the theoretical decay bound, and temporal self-convergence approaching the expected order $2 - \alpha$. An auxiliary three-mode benchmark embeds a globally Lipschitz saturated Lorenz vector field in the constrained partial differential equation (PDE) state space. Its double-scroll geometry, median 0–1 statistic $K_{01} = 0.993$, finite-time sensitivity, and synchronization demonstrate compatibility with chaotic invariant-modal dynamics; no claim of high-dimensional diffusion-generated spatiotemporal chaos is made.

Keywords: Caputo derivative; fractional reaction–diffusion system; integral moment constraints; constrained diffusion operator; synchronization; Mittag–Leffler stability; invariant-modal chaos
Mathematics Subject Classification: 35K58, 35R11, 47D06, 65M70, 93D20

1. Introduction

Fractional evolution equations provide a natural language for diffusion, transport, viscoelasticity, and nonlinear dynamics with memory. Standard monographs include [1, 2], while complementary analytical frameworks are presented in [3,4]. For spatially distributed models, the interaction between a Caputo time derivative and an unbounded elliptic operator requires an operator-theoretic or variational treatment; replacing the elliptic operator by a bounded map in L^2 is generally invalid. Therefore, fractional diffusion-wave equations and abstract fractional Cauchy problems have been studied by resolvent-family, spectral, and energy methods [5–7].

A second line of research concerns nonlocal constraints. Integral boundary and moment conditions arise only when the total mass, weighted averages, or aggregated measurements are prescribed. Recent existence studies treat fractional differential equations with nonlocal or integral data [8, 9]. Related fractional parabolic problems with nonclassical or nonlocal conditions are considered in [10,11]. Such constraints must be incorporated into a precisely defined state space or weak formulation; merely appending them to an unspecified operator domain does not determine a closed elliptic realization.

Fractional spatiotemporal dynamics have also been investigated in reaction–diffusion, optical, and transport settings. Chaotic and spatiotemporal oscillations in a fractional reaction–diffusion system were studied numerically in [12], while a Caputo predator–prey diffusion model with pattern formation was considered in [13]. Fractional optical systems exhibit controllable beam and soliton dynamics [14, 15]. These works demonstrate the variety of spatially distributed fractional dynamics, but they do not address synchronization under integral moment constraints.

A substantial numerical literature is devoted to time-fractional partial differential equations (PDEs) and memory-dependent fluid models. Representative contributions include nonlinear fractional heat transport in porous media [16], a space–time Caputo Cattaneo–Friedrich Maxwell model [17], distributed-order magnetohydrodynamic (MHD) simulations [18, 19], and a finite-element/finite-difference analysis of a coupled fractional viscoelastic model [20]. Classical predictor–corrector time stepping for fractional differential equations was developed in [21], while a high-order space–time spectral discretization for fractional PDEs was proposed in [22]. These studies motivate the numerical treatment adopted below, but none of them combine a rigorous moment-constrained operator, gradient-dependent synchronization analysis, and exact numerical enforcement of the same two integral constraints.

Synchronization of fractional chaotic systems is often studied in finite-dimensional settings [23, 24]. Related work on reaction–diffusion systems, spatiotemporal networks, and fractional chaotic neural networks appears in [25–27]. A direct transfer of those arguments to a fractional PDE with a derivative-dependent nonlinearity is not automatic: the error estimate contains $\|e_x\|$, the elliptic operator is unbounded, and long-time synchronization requires a global-in-time solution.

The present paper resolves these issues for a constrained semilinear reaction–diffusion drive–response system. The theorem-level contributions are as follows.

(C1) We define the homogeneous moment space $\mathcal{H}$, prove that $\mathcal{V} = H^1(0,1) \cap \mathcal{H}$ is dense in $\mathcal{H}$, establish a Poincaré inequality under the integral constraints, and construct the positive self-adjoint diffusion operator by a closed form. A strong characterization of $D(\mathcal{A})$ is given.

(C2) We handle nonhomogeneous moments through an explicit lifting and formulate the constrained

PDE by orthogonal projection. Equivalently, the strong equation contains two time-dependent Lagrange multipliers that enforce the moments.

(C3) We prove global well-posedness in the energy space $D(\mathcal{A}^{1/2})$ by fractional resolvent estimates and a Bielecki norm. This avoids both the false estimate $\|\mathcal{A}w\| \leq C\,\|w\|$ and an invalid local "restart" of the Caputo derivative.

(C4) We derive an explicit synchronization threshold that retains and absorbs the gradient mismatch. The resulting Mittag–Leffler estimate holds on $[0,\infty)$.

(C5) We validate the full constrained PDE with a spectral–L1 scheme whose basis satisfies both moments exactly. The local reaction–diffusion experiment includes parameter studies, threshold verification, comparison with the theoretical bound, and a corrected temporal self-convergence test. As a separate auxiliary benchmark, we embed a globally Lipschitz chaotic vector field in three admissible spatial modes. This verifies compatibility with chaotic invariant-modal dynamics, while explicitly avoiding a claim of high-dimensional diffusion-generated spatiotemporal chaos.

The term "purely integral boundary conditions" in the title refers to the two integral moment constraints as the essential nonlocal data imposed on the state. The no-flux relations appearing in the strong domain are natural boundary relations selected by the form, not additional independently prescribed boundary data; see Remark 3. This distinction is maintained throughout the operator formulation and the numerical discretization.

2. Integral constraints, projection, and lifting

For $w \in L^2(0,1)$, define

$$\mathcal{M}_0 w := \int_0^1 w(x)\,dx, \qquad \mathcal{M}_1 w := \int_0^1 x w(x)\,dx. \tag{2.1}$$

Let

$$\mathcal{H} := \{w \in L^2(0,1) : \mathcal{M}_0 w = \mathcal{M}_1 w = 0\}, \qquad \mathcal{V} := H^1(0,1) \cap \mathcal{H}. \tag{2.2}$$

Both spaces are equipped with their natural real Hilbert structures. The Gram matrix of 1 and x is

$$G = \begin{pmatrix} 1 & 1/2 \\ 1/2 & 1/3 \end{pmatrix}, \qquad G^{-1} = \begin{pmatrix} 4 & -6 \\ -6 & 12 \end{pmatrix}. \tag{2.3}$$

Hence, the orthogonal projection $\mathcal{P} : L^2(0,1) \to \mathcal{H}$ is explicitly

$$\mathcal{P}f = f - (1,x)G^{-1}\begin{pmatrix} \mathcal{M}_0 f \\ \mathcal{M}_1 f \end{pmatrix}, \tag{2.4}$$

where $(1,x)$ denotes the row vector of functions.

Lemma 1 (Density and constrained Poincaré inequality)**.** *The space $\mathcal{V}$ is dense in $\mathcal{H}$. Moreover,*

$$\|w\|_{L^2} \leq \frac{1}{\pi}\,\|w_x\|_{L^2}\,, \qquad w \in \mathcal{V}. \tag{2.5}$$

Proof. Let $f \in \mathcal{H}$. Choose $f_n \in C^\infty([0,1])$ with $f_n \to f$ in L^2. Since $\mathcal{P}$ is bounded on L^2 and maps smooth functions to smooth functions, $\mathcal{P}f_n \in \mathcal{V}$ and $\mathcal{P}f_n \to \mathcal{P}f = f$. Thus, $\mathcal{V}$ is dense in $\mathcal{H}$.

Every $w \in \mathcal{V}$ has a zero mean. The sharp one-dimensional Neumann Poincaré inequality for zero-mean functions gives (2.5). The second moment constraint is additional and does not weaken the estimate. ◻

Lemma (Surjectivity of the trace on the constrained energy space)**.** *The trace map*

$$\mathrm{Tr} : \mathcal{V} \longrightarrow \mathbb{R}^2, \qquad \mathrm{Tr}\, z = (z(0), z(1)),$$

is onto. More precisely, define

$$\psi_0(x) = 1 - 9x + 18x^2 - 10x^3, \qquad \psi_1(x) = 3x - 12x^2 + 10x^3.$$

A direct calculation gives

$$\mathcal{M}_0\psi_i = \mathcal{M}_1\psi_i = 0, \qquad (\psi_0(0), \psi_0(1)) = (1, 0), \qquad (\psi_1(0), \psi_1(1)) = (0, 1).$$

Hence, for an arbitrary $(r_0, r_1) \in \mathbb{R}^2$, the function $z = r_0\psi_0 + r_1\psi_1$ belongs to $\mathcal{V}$ and satisfies $\mathrm{Tr}\, z = (r_0, r_1)$*. Thus, the admissible trace space of $\mathcal{V}$ is the whole of* $\mathbb{R}^2$.

We allow prescribed moment data

$$\mathcal{M}_0 u(t) = m_0(t), \qquad \mathcal{M}_1 u(t) = m_1(t), \tag{2.6}$$

with the same functions m_0, m_1 for the drive and response. An explicit no-flux lifting is

$$\chi(x,t) = m_0(t) + \frac{\pi^2}{4}(m_0(t) - 2m_1(t)) \cos(\pi x). \tag{2.7}$$

Indeed, $\mathcal{M}_0\chi = m_0$, $\mathcal{M}_1\chi = m_1$, and $\chi_x(0,t) = \chi_x(1,t) = 0$. Thus, $U = u - \chi$ and $V = v - \chi$ belong to $\mathcal{H}$ for every t.

3. The constrained diffusion operator

Assume throughout that

$$a \in W^{1,\infty}(0,1), \qquad 0 < a_0 \le a(x) \le a_1 < \infty. \tag{3.1}$$

Define the symmetric bilinear form

$$\mathfrak{a}(w,z) := \int_0^1 a(x) w_x(x) z_x(x)\, dx, \qquad w, z \in \mathcal{V}. \tag{3.2}$$

By Lemma 1,

$$\mathfrak{a}(w,w) \ge a_0 \|w_x\|_{L^2}^2 \ge a_0\pi^2 \|w\|_{L^2}^2 . \tag{3.3}$$

The form is densely defined, closed, symmetric, and coercive on $\mathcal{H}$.

Definition 1 (Form realization)**.** *The operator $\mathcal{A} : D(\mathcal{A}) \subset \mathcal{H} \to \mathcal{H}$ associated with* (3.2) *is defined by*

$$D(\mathcal{A}) := \{w \in \mathcal{V} : \exists f \in \mathcal{H} \text{ such that } \mathfrak{a}(w, z) = \langle f, z\rangle_{L^2}\ \forall z \in \mathcal{V}\}, \qquad \mathcal{A}w = f. \tag{3.4}$$

Proposition 2 (Operator properties and strong domain)**.** *The operator $\mathcal{A}$ is positive self-adjoint, $D(\mathcal{A})$ is dense in $\mathcal{H}$, $\mathcal{A}^{-1}$ is compact, and $-\mathcal{A}$ generates an analytic contraction semigroup on $\mathcal{H}$. Furthermore,*

$$D(\mathcal{A}) = \left\{w \in H^2(0, 1) \cap \mathcal{H} : a(0)w_x(0) = a(1)w_x(1) = 0\right\}, \tag{3.5}$$

with

$$\mathcal{A}w = \mathcal{P}[-(aw_x)_x]. \tag{3.6}$$

Finally,

$$D(\mathcal{A}^{1/2}) = \mathcal{V}, \qquad \left\|\mathcal{A}^{1/2}w\right\|_{L^2}^2 = \mathfrak{a}(w, w), \tag{3.7}$$

and the first eigenvalue satisfies $\lambda_1(\mathcal{A}) \geq a_0\pi^2$.

Proof. The first assertions follow from the representation theorem for densely defined closed coercive symmetric forms and the compact embedding $\mathcal{V} \hookrightarrow \mathcal{H}$. Identity (3.7) is the square-root identity for a positive self-adjoint form realization.

Let $w \in H^2(0, 1) \cap \mathcal{H}$ satisfy the flux relations in (3.5). Integration by parts gives

$$\mathfrak{a}(w, z) = \int_0^1 -(aw_x)_x z\, dx = \langle \mathcal{P}[-(aw_x)_x], z\rangle_{L^2}, \qquad z \in \mathcal{V},$$

because $z \in \mathcal{H}$. Hence, $w \in D(\mathcal{A})$ and (3.6) holds.

Conversely, let $w \in D(\mathcal{A})$ and let $f = \mathcal{A}w \in \mathcal{H}$. The continuous functional

$$\mathcal{L}(z) := \mathfrak{a}(w, z) - \langle f, z\rangle_{L^2}, \qquad z \in H^1(0, 1),$$

vanishes on $\mathcal{V} = \ker \mathcal{M}_0 \cap \ker \mathcal{M}_1$. Since the moment map $z \mapsto (\mathcal{M}_0 z, \mathcal{M}_1 z)$ is onto $\mathbb{R}^2$ (its Gram matrix is the invertible matrix G in (2.3)), the quotient-space factorization theorem yields constants $c_0, c_1 \in \mathbb{R}$ such that

$$\mathcal{L}(z) = c_0\mathcal{M}_0 z + c_1\mathcal{M}_1 z, \qquad z \in H^1(0, 1).$$

Testing this identity with $z \in C_c^\infty(0, 1)$ gives, in distributions,

$$-(aw_x)_x = f + c_0 + c_1 x.$$

The right-hand side belongs to $L^2(0, 1)$. Since $a \in W^{1,\infty}(0, 1)$ is uniformly positive, one-dimensional elliptic regularity gives $w \in H^2(0, 1)$. Integrating by parts and returning to test functions $z \in \mathcal{V}$ now gives

$$a(1)w_x(1)z(1) - a(0)w_x(0)z(0) = 0, \qquad z \in \mathcal{V}.$$

The preceding trace-surjectivity lemma permits the independent choices $(z(0), z(1)) = (1, 0)$ and $(0, 1)$; hence, $a(0)w_x(0) = a(1)w_x(1) = 0$. Finally, $f \in \mathcal{H}$, $f = \mathcal{P}[-(aw_x)_x]$, which proves (3.6). The eigenvalue estimate follows from (3.3) and the Rayleigh quotient. □

Remark 3 (Meaning of the natural flux relations)**.** *The essential state restrictions are the two integral moments in* (2.2)*. The endpoint flux relations in* (3.5) *arise from the form realization, exactly as homogeneous Neumann conditions arise from the standard H^1 energy form. Therefore, they are natural relations of the weak operator, not separately imposed pointwise data replacing the moment constraints.*

4. Drive–response system and mild formulation

Let $0 < \alpha < 1$. In the original variables, the constrained drive–response system is understood in projected form. After the lifting (2.7), the homogeneous variables $U = u - \chi$ and $V = v - \chi$ satisfy

$$ {}^C D_t^\alpha U + \mathcal{A} U = \mathcal{N}(t, U) + g_\chi(t), \tag{4.1} $$

$$ {}^C D_t^\alpha V + \mathcal{A} V = \mathcal{N}(t, V) + g_\chi(t) + K(U - V), \tag{4.2} $$

with $U(0) = U_0 \in \mathcal{V}$, $V(0) = V_0 \in \mathcal{V}$, where

$$ \mathcal{N}(t, w) := \mathcal{P} F(\cdot, t, w + \chi, (w + \chi)_x), \tag{4.3} $$

$$ g_\chi(t) := -\mathcal{P}\left({}^C D_t^\alpha \chi - (a\chi_x)_x \right). \tag{4.4} $$

Equivalently, in strong notation, the unprojected equation contains a term $\lambda_0(t) + \lambda_1(t)x$; the two multipliers are uniquely selected so that (2.6) holds. This is the standard constrained-evolution interpretation of the two moment conditions.

We impose the following assumptions.

Assumption 4 (Gradient-dependent nonlinearity). *The function $F : (0, 1) \times [0, \infty) \times \mathbb{R} \times \mathbb{R} \to \mathbb{R}$ is measurable in (x, t) and continuous in (r, p). There exist constants $L_0, L_1 \geq 0$ such that*

$$ |F(x, t, r_1, p_1) - F(x, t, r_2, p_2)| \leq L_0 |r_1 - r_2| + L_1 |p_1 - p_2| \tag{4.5} $$

for almost every (x, t) and all r_i, p_i. In addition, $F(\cdot, t, 0, 0)$ is locally bounded in $L^2(0, 1)$ uniformly in t.

Assumption 5 (Moment data). *The functions m_0, m_1 are locally absolutely continuous, and their Caputo derivatives are locally bounded on $[0, \infty)$. Consequently, $g_\chi \in L^\infty_{\mathrm{loc}}([0, \infty); \mathcal{H})$.*

By (4.5), (3.7), and the boundedness of $\mathcal{P}$,

$$ \|\mathcal{N}(t, w) - \mathcal{N}(t, z)\|_{\mathcal{H}} \leq C_N \|w - z\|_{\mathcal{V}}, \qquad C_N := C(a_0)(L_0 + L_1). \tag{4.6} $$

Remark 6 (Abstract admissible nonlinearities). *The pointwise representation (4.3) is a sufficient, but not necessary, realization of the theory. All well-posedness and synchronization arguments below remain valid if $\mathcal{N}(t, \cdot) : \mathcal{V} \to \mathcal{H}$ is any (possibly finite-rank or nonlocal) map satisfying, locally uniformly in t,*

$$ \|\mathcal{N}(t, w) - \mathcal{N}(t, z)\|_{\mathcal{H}} \leq C_N \|w - z\|_{\mathcal{V}}, \tag{4.7} $$

$$ \langle \mathcal{N}(t, w) - \mathcal{N}(t, z), w - z \rangle_{L^2} \leq L_0 \|w - z\|_{L^2}^2 + L_1 \|(w - z)_x\|_{L^2} \|w - z\|_{L^2}. \tag{4.8} $$

The local gradient-dependent nonlinearity in Assumption 4 satisfies these estimates. The finite-rank chaotic benchmark in Section 8 satisfies them with $L_1 = 0$ because its saturated modal vector field is globally Lipschitz.

For the positive self-adjoint operator $\mathcal{A}$, define the fractional solution operators by spectral calculus,

$$ S_\alpha(t) := E_\alpha(-t^\alpha \mathcal{A}), \qquad P_\alpha(t) := t^{\alpha-1} E_{\alpha,\alpha}(-t^\alpha \mathcal{A}). \tag{4.9} $$

For $0 \leq \theta \leq 1$, they satisfy

$$ \left\| \mathcal{A}^\theta S_\alpha(t) \right\|_{\mathcal{L}(\mathcal{H})} \leq C_\theta t^{-\alpha\theta}, \qquad \left\| \mathcal{A}^\theta P_\alpha(t) \right\|_{\mathcal{L}(\mathcal{H})} \leq C_\theta t^{\alpha-1-\alpha\theta}. \tag{4.10} $$

Definition 2 (Energy-space mild solution)**.** *A pair* $(U,V) \in C([0,T];\mathcal{V})^2$ *is a mild solution of* (4.1)–(4.2) *if*

$$U(t) = S_\alpha(t)U_0 + \int_0^t P_\alpha(t-s)[\mathcal{N}(s,U(s)) + g_\chi(s)]ds, \tag{4.11}$$

$$V(t) = S_\alpha(t)V_0 + \int_0^t P_\alpha(t-s)[\mathcal{N}(s,V(s)) + g_\chi(s) + K(U(s)-V(s))]ds. \tag{4.12}$$

5. Global well-posedness

Theorem 7 (Global energy-space well-posedness)**.** *Assume* (3.1)*, Assumption 5, and either Assumption 4 or the abstract estimates* (4.7)–(4.8)*. For every* $U_0, V_0 \in \mathcal{V}$ *and every* $T > 0$*, System* (4.1)–(4.2) *admits a unique mild solution*

$$(U,V) \in C([0,T];\mathcal{V})^2. \tag{5.1}$$

The solutions obtained for different T *are consistent by uniqueness and therefore define a unique global solution on* $[0,\infty)$*. Moreover, for each finite* T*,*

$$\sup_{0\le t\le T} (\|U(t)\|_{\mathcal{V}} + \|V(t)\|_{\mathcal{V}}) \le C_T \left(1 + \|U_0\|_{\mathcal{V}} + \|V_0\|_{\mathcal{V}} + \left\|g_\chi\right\|_{L^\infty(0,T;\mathcal{H})}\right). \tag{5.2}$$

Proof. Set $X_T = C([0,T];\mathcal{V})^2$ and define the right-hand side of (4.11)–(4.12) as a map $\Phi : X_T \to X_T$. The continuity at $t=0$ follows from the strong continuity of S_α on $\mathcal{V}$ and from the integrability of the kernel in (4.10) with $\theta = 1/2$:

$$\left\|\mathcal{A}^{1/2}P_\alpha(t)\right\| \le Ct^{\alpha/2-1}, \qquad \alpha/2 - 1 > -1. \tag{5.3}$$

Thus, Φ maps X_T into itself.

For $\beta > 0$, use the Bielecki norm

$$\|(U,V)\|_\beta := \sup_{0\le t\le T} e^{-\beta t}(\|U(t)\|_{\mathcal{V}} + \|V(t)\|_{\mathcal{V}}). \tag{5.4}$$

By (4.6), (5.3), and the boundedness of the coupling $K : \mathcal{V} \to \mathcal{H}$,

$$\begin{aligned}\|\Phi(U_1,V_1) - \Phi(U_2,V_2)\|_\beta &\le C(C_N + 2K)\sup_{t\le T}\int_0^t e^{-\beta(t-s)}(t-s)^{\alpha/2-1}ds \\ &\qquad \times \|(U_1-U_2, V_1-V_2)\|_\beta \\ &\le C(C_N+2K)\Gamma(\alpha/2)\beta^{-\alpha/2}\,\|(U_1-U_2,V_1-V_2)\|_\beta\,. \end{aligned}\tag{5.5}$$

Choose β so large that the last coefficient is less than one. Then, Banach's fixed-point theorem yields a unique mild solution on the entire prescribed interval $[0,T]$. No boundedness assumption on $\mathcal{A}$ is used, and no restart of the Caputo derivative is involved.

Applying the same convolution estimate to the fixed point, followed by the fractional Gronwall inequality with exponent $\alpha/2$, gives (5.2). Since the argument applies to every finite T, and uniqueness makes the restrictions consistent, the solution is global on $[0,\infty)$. □

Lemma (Spectral Galerkin approximation in the energy space)**.** *Let $(e_j, \lambda_j)_{j\geq 1}$ be the orthonormal eigenpairs of $\mathcal{A}$, and let Q_n be the orthogonal projection onto $H_n = \mathrm{span}\{e_1, \ldots, e_n\}$. On every finite interval $[0, T]$, the projected systems*

$$
\begin{aligned}
{}^{C}D_t^{\alpha} U_n + \mathcal{A} U_n &= Q_n \mathcal{N}(t, U_n) + Q_n g_{\chi}, \\
{}^{C}D_t^{\alpha} V_n + \mathcal{A} V_n &= Q_n \mathcal{N}(t, V_n) + Q_n g_{\chi} + K(U_n - V_n),
\end{aligned}
$$

with initial values $Q_n U_0, Q_n V_0$, have unique finite-dimensional solutions and

$$(U_n, V_n) \longrightarrow (U, V) \quad \text{in } C([0, T]; \mathcal{V})^2.$$

Indeed, Q_n commutes with the spectral families $S_{\alpha}(t)$ and $P_{\alpha}(t)$ and is a contraction in both $\mathcal{H}$ and $\mathcal{V}$. Therefore, the Bielecki contraction estimate (5.5) *holds with a contraction constant independent of n. If Φ_n and Φ denote the projected and limiting fixed-point maps, respectively, then*

$$\|(U_n, V_n) - (U, V)\|_{\beta} \leq \frac{1}{1 - q} \|\Phi_n(U, V) - \Phi(U, V)\|_{\beta},$$

where $q < 1$ is independent of n. Strong convergence $Q_n \to I$ in $\mathcal{H}$ and $\mathcal{V}$, together with the resolvent bounds and dominated convergence for the convolution terms, makes the right-hand side tend to zero.

Remark 8 (Strong solutions and energy estimates)**.** *If $U_0, V_0 \in D(\mathcal{A})$ and the data have the standard additional time regularity, then the mild solution is strong for $t > 0$. For general energy-space data, the preceding spectral Galerkin lemma supplies strongly convergent finite-dimensional approximations. The synchronization estimate is proven for these approximations. Then, its already-integrated Mittag–Leffler bound is passed directly to the limit in $C([0, T]; \mathcal{H})$; no formal inner product is applied to an insufficiently regular mild solution.*

6. Mittag–Leffler synchronization

Let

$$E(t) := V(t) - U(t). \tag{6.1}$$

Because the drive and response have the same moment data, $E(t) \in \mathcal{H}$ and satisfies homogeneous moment constraints. Subtracting (4.1) from (4.2) gives

$${}^{C}D_t^{\alpha} E + \mathcal{A} E = \mathcal{N}(t, V) - \mathcal{N}(t, U) - KE. \tag{6.2}$$

For the local realization (4.3), the difference on the right is precisely the projected difference of the two pointwise nonlinearities.

Theorem 9 (Explicit synchronization threshold)**.** *Assume the hypotheses of Theorem 7. Fix $\delta \in (0, 1)$ and define*

$$\mu_{\delta} := K + (1 - \delta) a_0 \pi^2 - L_0 - \frac{L_1^2}{4 \delta a_0}. \tag{6.3}$$

If $\mu_{\delta} > 0$, then for all $t \geq 0$,

$$\|V(t) - U(t)\|_{L^2}^2 \leq E_{\alpha}(-2\mu_{\delta} t^{\alpha}) \|V_0 - U_0\|_{L^2}^2. \tag{6.4}$$

Consequently,

$$\|V(t) - U(t)\|_{L^2} \longrightarrow 0 \qquad (t \to \infty), \tag{6.5}$$

and the synchronization is of Mittag–Leffler type.

Proof. Let U_n, V_n be the spectral Galerkin solutions from the preceding lemma and set $E_n = V_n - U_n$. The standard Caputo convexity inequality gives

$$\frac{1}{2}\,{}^{C}D_t^{\alpha}\,\|E_n(t)\|_{L^2}^2 \le \left\langle {}^{C}D_t^{\alpha} E_n(t), E_n(t)\right\rangle_{L^2}. \tag{6.6}$$

Taking the L^2 inner product of the Galerkin error equation with E_n and using $E_n \in \mathcal{H}$ yields

$$\frac{1}{2}\,{}^{C}D_t^{\alpha}\,\|E_n\|^2 + \int_0^1 a|E_{n,x}|^2 dx + K\,\|E_n\|^2 \le L_0\,\|E_n\|^2 + L_1\,\left\|E_{n,x}\right\|\,\|E_n\|. \tag{6.7}$$

Rather than replacing the last term by an unexplained "effective constant", Young's inequality gives, for the selected $\delta \in (0,1)$,

$$L_1\,\left\|E_{n,x}\right\|\,\|E_n\| \le \delta a_0\,\left\|E_{n,x}\right\|^2 + \frac{L_1^2}{4\delta a_0}\,\|E_n\|^2. \tag{6.8}$$

Using $a \ge a_0$ and the constrained Poincaré inequality (2.5), the unabsorbed diffusion satisfies

$$(1-\delta)a_0\,\left\|E_{n,x}\right\|^2 \ge (1-\delta)a_0\pi^2\,\|E_n\|^2. \tag{6.9}$$

Therefore, with $y_n(t) = \|E_n(t)\|^2$,

$${}^{C}D_t^{\alpha} y_n(t) + 2\mu_\delta y_n(t) \le 0. \tag{6.10}$$

The scalar fractional comparison principle gives

$$y_n(t) \le E_\alpha(-2\mu_\delta t^\alpha) y_n(0), \qquad 0 \le t \le T. \tag{6.11}$$

By the spectral Galerkin lemma, $E_n \to E$ in $C([0,T];\mathcal{V})$ and $E_n(0) \to E(0)$ in $\mathcal{H}$. Therefore, passing to the limit in this scalar inequality yields (6.4) on $[0,T]$. Since $T > 0$ is arbitrary, the estimate holds for every $t \ge 0$. Finally, $\mu_\delta > 0$ and $0 < \alpha < 1$ imply $E_\alpha(-2\mu_\delta t^\alpha) \to 0$ as $t \to \infty$. □

Corollary 10 (Practical design rule)**.** *A sufficient gain is*

$$K > K_{\mathrm{th}}(\delta) := L_0 + \frac{L_1^2}{4\delta a_0} - (1-\delta)a_0\pi^2 \tag{6.12}$$

for at least one $\delta \in (0,1)$. The bound is sufficient, not necessary; numerical synchronization may occur below it because the actual spectral gap or nonlinear behavior can be more favorable than the global estimates.

7. A nontrivial PDE example with complete hypothesis verification

Example 11 (Constrained fractional reaction–diffusion pair)**.** *Let* $a = 0.02$*,* $\rho = 1.2$*,* $\eta = 0.05$*, and*

$$q(x,t) = 0.8\cos(2\pi x)\cos(0.7t) + 0.4\cos(4\pi x)\sin(0.5t). \tag{7.1}$$

Consider the homogeneous moment constraints

$$\int_0^1 u(x,t)dx = \int_0^1 xu(x,t)dx = 0, \qquad \int_0^1 v(x,t)dx = \int_0^1 xv(x,t)dx = 0, \tag{7.2}$$

and the projected equations

$${}^C D_t^\alpha u - 0.02u_{xx} = \mathcal{P}\left[1.2\sin u + 0.05\sin(2\pi x)u_x + q(x,t)\right], \tag{7.3}$$

$${}^C D_t^\alpha v - 0.02v_{xx} = \mathcal{P}\left[1.2\sin v + 0.05\sin(2\pi x)v_x + q(x,t)\right] + K(u-v). \tag{7.4}$$

The initial data are

$$u(x,0) = 0.8\cos(2\pi x) + 0.35\cos(4\pi x), \tag{7.5}$$

$$v(x,0) = -0.6\cos(2\pi x) + 0.2\cos(6\pi x). \tag{7.6}$$

Each function $\cos(2j\pi x)$ *has vanishing zeroth and first moments, so the initial data satisfy* (7.2)*. The diffusion coefficient satisfies* (3.1) *with* $a_0 = a_1 = 0.02$*. Since* $|\sin r_1 - \sin r_2| \le |r_1 - r_2|$ *and* $|\sin(2\pi x)| \le 1$*, Assumption 4 holds globally with*

$$L_0 = 1.2, \qquad L_1 = 0.05. \tag{7.7}$$

The forcing q is smooth and has both moments equal to zero. Thus, Theorem 7 applies globally without truncation or an unproved invariant-region argument.

For $\delta = 1/2$*, Corollary 10 gives*

$$K_{\text{th}} = 1.2 + \frac{0.05^2}{2(0.02)} - \frac{0.02\pi^2}{2} \approx 1.163804. \tag{7.8}$$

Hence, $K = 1.2, 1.5, 2.0$ *are rigorously certified by Theorem 9, while* $K = 0, 0.5, 1.0$ *are below the sufficient analytical threshold.*

8. An auxiliary constraint-preserving chaotic modal benchmark

The preceding local reaction–diffusion example verifies every hypothesis of the main theorem and is the principal analytical and numerical validation. Now, we add a separate finite-rank benchmark on the same constrained state space to test whether the operator framework, moment constraints, and coupling mechanism remain compatible with chaotic invariant-modal dynamics. The spatial operator, integral constraints, and field reconstruction are retained, while the first three admissible modes carry a globally Lipschitz saturated fractional Lorenz vector field. This auxiliary construction is deliberately finite-dimensional on its invariant manifold; it is not presented as evidence of high-dimensional spatiotemporal chaos generated by diffusion.

Let

$$\phi_j(x) = \sqrt{2}\cos(2j\pi x), \qquad j = 1, 2, 3, \tag{8.1}$$

and define

$$z_j(w) := \left\langle w, \phi_j \right\rangle_{L^2}, \qquad j = 1, 2, 3. \tag{8.2}$$

Define the smooth saturation

$$S_R(s) := R\tanh(s/R). \tag{8.3}$$

For $z = (z_1, z_2, z_3)^\top$, set

$$f_R(z) := \begin{pmatrix} \sigma(z_2 - z_1) \\ \rho z_1 - z_2 - S_R(z_1)S_R(z_3) \\ S_R(z_1)S_R(z_2) - \beta z_3 \end{pmatrix}, \qquad (\sigma, \rho, \beta) = (10, 28, 8/3). \tag{8.4}$$

Writing $\lambda_j = 0.02(2j\pi)^2$, define the finite-rank reaction operator

$$C_R(w) := \sum_{j=1}^{3} \left[f_{R,j}(z(w)) + \lambda_j z_j(w) \right] \phi_j. \tag{8.5}$$

We study

$$^C D_t^\alpha u + \mathcal{A}u = C_R(u), \tag{8.6}$$

$$^C D_t^\alpha v + \mathcal{A}v = C_R(v) + K(u - v), \tag{8.7}$$

under the homogeneous moments (7.2). Since S_R is bounded and $|S_R'| \leq 1$, f_R and C_R are globally Lipschitz. Hence, Remark 6 applies with $L_1 = 0$, and the equations are globally well posed.

The subspace $E_3 = \operatorname{span}\{\phi_1, \phi_2, \phi_3\}$ is invariant. Indeed, if

$$u(x, t) = \sum_{j=1}^{3} z_j(t)\phi_j(x), \tag{8.8}$$

then the diffusion term $\lambda_j z_j \phi_j$ is canceled by the compensating term in (8.5), and the modal amplitudes solve the saturated fractional Lorenz system

$$^C D_t^\alpha z = f_R(z). \tag{8.9}$$

All higher modes satisfy homogeneous fractional diffusion equations and decay. Consequently, (8.6) is a moment-constrained PDE realization of a three-dimensional invariant chaotic subsystem, and the reconstructed field provides a spatial representation of those modal amplitudes. The compensating term in (8.5) cancels diffusion on the first three modes; accordingly, the example demonstrates compatibility and synchronization of constrained chaotic modal dynamics, not diffusion-generated high-dimensional spatiotemporal chaos. The saturation radius $R = 50$ preserves a Lorenz-type regime while retaining the global Lipschitz property required by the analytical framework.

9. Constraint-preserving numerical discretization

9.1. Common moment-preserving spectral Galerkin space

For Example 11, define

$$\phi_j(x) = \sqrt{2}\cos(2j\pi x), \qquad j = 1, \dots, N. \tag{9.1}$$

These functions are orthonormal in $L^2(0,1)$, satisfy the natural no-flux relations, and obey

$$\mathcal{M}_0\phi_j = \mathcal{M}_1\phi_j = 0. \tag{9.2}$$

Thus every Galerkin approximation

$$u_N(x,t) = \sum_{j=1}^{N} c_j(t)\phi_j(x), \qquad v_N(x,t) = \sum_{j=1}^{N} d_j(t)\phi_j(x) \tag{9.3}$$

fulfills both integral constraints exactly, without penalty parameters or post-processing. The diffusion matrix is diagonal with

$$\lambda_j = 0.02(2j\pi)^2. \tag{9.4}$$

The nonlinear coefficients are evaluated by midpoint spectral quadrature on 1024 points.

9.2. L1 time stepping for the local PDE in Example 1

Let $t_n = nh$, $n = 0, \dots, N_t$, and

$$b_k = (k+1)^{1-\alpha} - k^{1-\alpha}, \qquad \gamma_\alpha = \frac{1}{\Gamma(2-\alpha)h^\alpha}. \tag{9.5}$$

For a coefficient vector y^n, the L1 approximation is

$${}^{C}D_t^\alpha y(t_n) \approx \gamma_\alpha \left[y^n - y^{n-1} + \sum_{k=1}^{n-1} b_k (y^{n-k} - y^{n-k-1}) \right]. \tag{9.6}$$

Diffusion and linear coupling are treated implicitly, while the nonlinear projection is evaluated from the previous state. If $\Lambda = \mathrm{diag}(\lambda_1, \dots, \lambda_N)$ and $\mathbf{N}(t,y)$ denotes the projected nonlinear coefficient vector, then

$$(\gamma_\alpha I + \Lambda)c^n = \mathbf{N}(t_n, c^{n-1}) + \gamma_\alpha c^{n-1} - \gamma_\alpha \sum_{k=1}^{n-1} b_k (c^{n-k} - c^{n-k-1}), \tag{9.7}$$

$$(\gamma_\alpha I + \Lambda + KI)d^n = \mathbf{N}(t_n, d^{n-1}) + Kc^n + \gamma_\alpha d^{n-1} - \gamma_\alpha \sum_{k=1}^{n-1} b_k (d^{n-k} - d^{n-k-1}). \tag{9.8}$$

The algorithm, all parameters, and the source code are included with the revised source files.

9.3. Modal implementation of the chaotic PDE in Example 2

For (8.6)–(8.7), the same basis (9.1) is used. Because E_3 is invariant, the first three coefficient equations are advanced by the L1 formula, with the linear Lorenz part treated implicitly and the saturated products treated explicitly. Modes $j \geq 4$ only retain their diagonal fractional diffusion. The chaotic drive is computed with $\alpha = 0.98$, $R = 50$, $h = 0.01$, and $T = 100$. For the drive–response tests, $T = 40$ and the initial modal vectors are

$$z(0) = (1, 1, 1)^{\top}, \qquad \widetilde{z}(0) = (-8, 7, 20)^{\top}. \tag{9.9}$$

The reconstructed fields automatically satisfy both integral moments because every participating basis function belongs to $\mathcal{H}$.

10. Numerical results: two complementary PDE examples

The numerical study comprises two clearly separated examples with distinct purposes. Example 1 is the principal validation experiment: it discretizes the complete local reaction–diffusion drive–response PDE of Example 11, enforces the two integral constraints, and tests the analytical synchronization theorem, the gain threshold, fractional orders below 0.9, and numerical refinement. Example 2 then provides direct numerical evidence of a chaotic regime within the same moment-constrained PDE framework.

10.1. Example 1: full local reaction–diffusion PDE under integral moment constraints

This example applies the numerical method directly to Eqs (7.3)–(7.4), with the forcing, initial data, and moment conditions stated in Example 11. Unless stated otherwise, the parameters are

$$T = 4, \qquad h = 0.01, \qquad N = 8, \qquad M_q = 1024, \tag{10.1}$$

and the representative synchronized run uses $\alpha = 0.98$ and $K = 1.5$. The choice $K = 1.5$ lies above the sufficient theoretical threshold $K_{\text{th}} \approx 1.163804$ in (7.8). Thus, this example simultaneously tests the spatial diffusion operator, the derivative-dependent nonlinearity, the Caputo memory term, the drive–response coupling, and the two integral constraints.

10.1.1. Complete drive, response, and synchronization-error fields

Figures 1–3 show the full space–time evolution of the drive, the response, and their pointwise difference. The response starts from a substantially different initial profile, but the coupling progressively aligns it with the drive. The pointwise error becomes uniformly small over the spatial interval, rather than only at a selected observation point. These figures make explicit that the computation concerns the complete PDE fields $u_N(x, t)$ and $v_N(x, t)$.

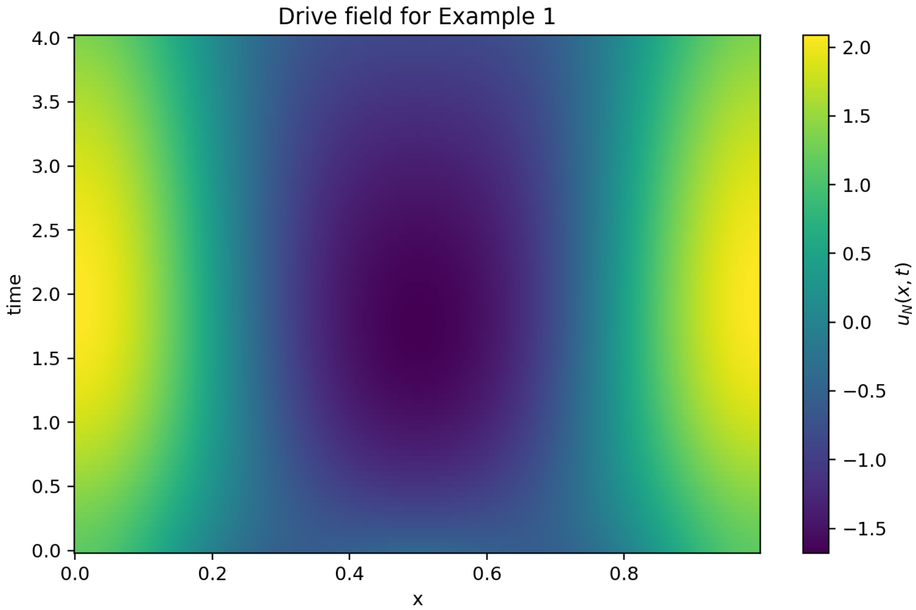

Figure 1. Example 1: spatiotemporal evolution of the full drive field $u_N(x,t)$ for $\alpha = 0.98$ and $K = 1.5$.

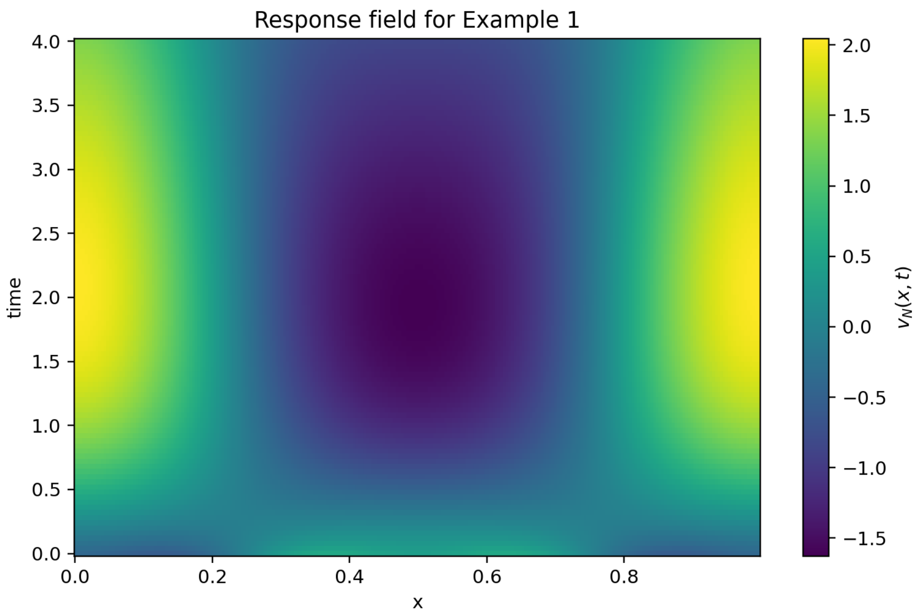

Figure 2. Example 1: spatiotemporal evolution of the full response field $v_N(x,t)$ for $\alpha = 0.98$ and $K = 1.5$.

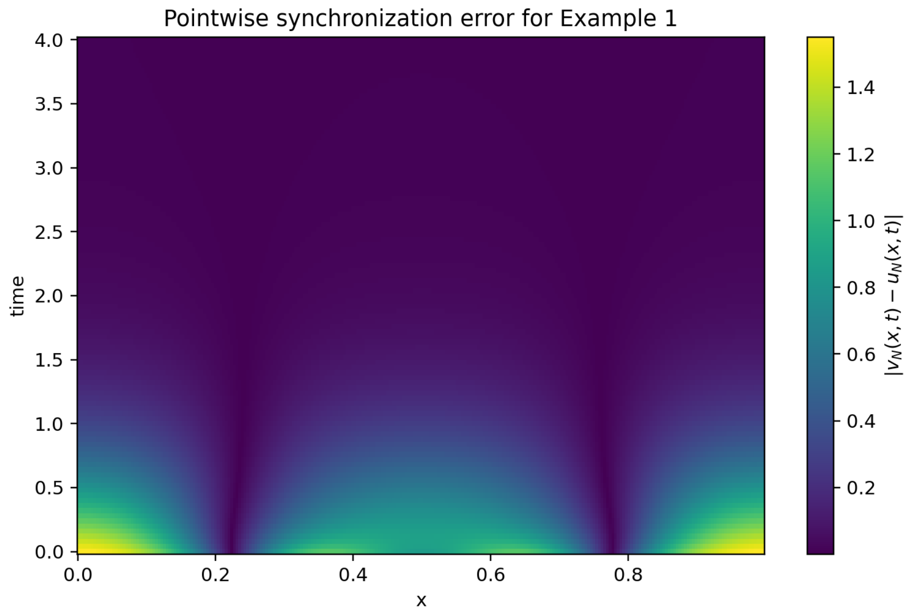

Figure 3. Example 1: pointwise synchronization error $|v_N(x,t) - u_N(x,t)|$. The initially different fields approach one another throughout the spatial domain.

10.1.2. Exact enforcement of the integral moments

For $\alpha = 0.98$ and $K = 1.5$, the maximum absolute moment residuals at the final time are

$$|\mathcal{M}_0 u_N| = 5.55 \times 10^{-17}, \quad |\mathcal{M}_1 u_N| = 6.94 \times 10^{-17}, \quad |\mathcal{M}_0 v_N| = 5.55 \times 10^{-17}, \quad |\mathcal{M}_1 v_N| = 2.78 \times 10^{-17}. \tag{10.2}$$

These values are at the level of floating-point roundoff and confirm that the discretization enforces the core integral constraints. Figure 4 compares the two complete spatial profiles at the final time.

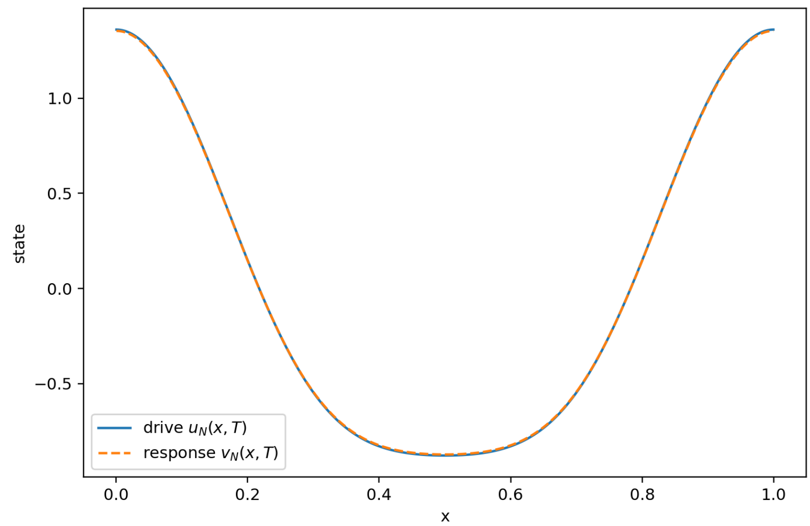

Figure 4. Example 1: drive and response PDE profiles at $T = 4$ for $\alpha = 0.98$ and $K = 1.5$. The two integral moments are preserved to machine precision.

10.1.3. Coupling gain and analytical threshold

Figure 5 and Table 1 show the full PDE synchronization error. The uncoupled pair retains a large error, whereas increasing K strongly accelerates tracking. Theorem 9 certifies all tests with $K > 1.163804$. The observed decay for $K = 1.0$ illustrates that the analytical threshold is sufficient rather than necessary.

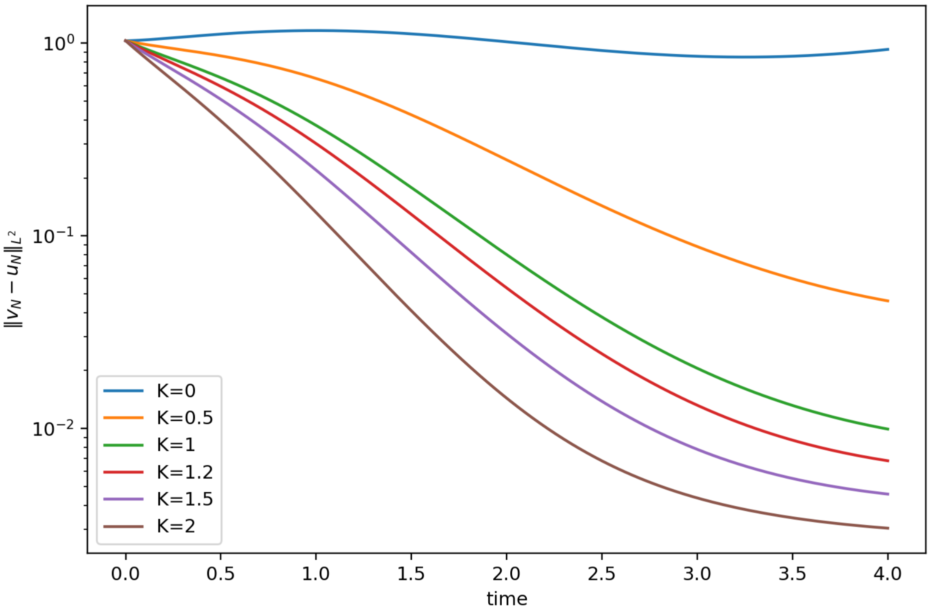

Figure 5. Example 1: full PDE synchronization error for different gains with $\alpha = 0.98$. The sufficient analytical threshold is $K_{\text{th}} \approx 1.163804$.

Table 1. Example 1: influence of the coupling gain for the constrained PDE at $\alpha = 0.98$.

K	Relative to K_{th}	Final error	Mean, last 50 steps	Interpretation
0.0	below	9.2913×10^{-1}	9.3450×10^{-1}	no synchronization
0.5	below	4.5998×10^{-2}	5.2010×10^{-2}	slow decay
1.0	below	9.9414×10^{-3}	1.1313×10^{-2}	observed, not certified
1.2	above	6.8064×10^{-3}	7.6044×10^{-3}	certified by the theorem
1.5	above	4.5704×10^{-3}	4.9619×10^{-3}	certified by the theorem
2.0	above	3.0400×10^{-3}	3.2105×10^{-3}	fastest tested decay

10.1.4. Fractional orders below 0.9

The choice $\alpha = 0.98$ represents a weak-memory regime close to the classical first-order derivative and allows for comparison with earlier near-integer simulations. It is not assumed to be universal. To test a stronger memory, Figure 6 and Table 2 include $\alpha = 0.85$ and $\alpha = 0.75$. Synchronization persists for all three orders at $K = 1.5$, but a smaller α produces a longer algebraic memory tail and a larger finite-time error.

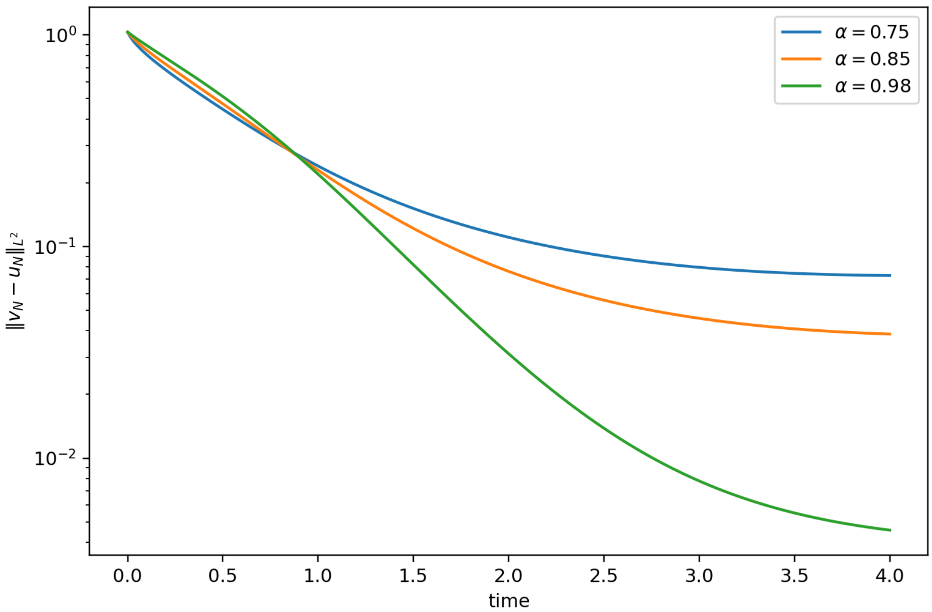

Figure 6. Example 1: full PDE synchronization for $\alpha = 0.75, 0.85, 0.98$ with $K = 1.5$.

Table 2. Example 1: influence of the fractional order at $K = 1.5$.

α	Final error	Mean error on last 50 steps
0.75	7.2881×10^{-2}	7.3562×10^{-2}
0.85	3.8567×10^{-2}	3.9504×10^{-2}
0.98	4.5704×10^{-3}	4.9619×10^{-3}

10.1.5. Comparison with the Mittag–Leffler bound

For $\alpha = 0.98$, $K = 1.5$, and $\delta = 1/2$, Formula (6.3) gives $\mu_{1/2} = 0.336196$. Figure 7 compares the computed squared error with

$$E_{0.98}(-2\mu_{1/2}t^{0.98})\, \|v_N(0) - u_N(0)\|^2 . \tag{10.3}$$

The numerical curve remains below the theoretical upper bound. The gap is expected because the proof uses the global constants L_0, L_1, and the conservative Poincaré lower bound $a_0\pi^2$.

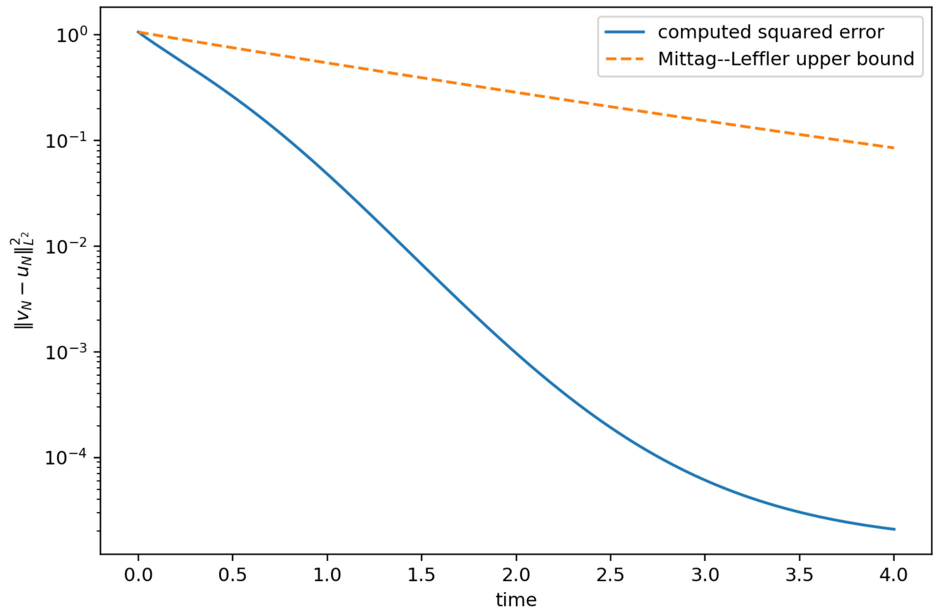

Figure 7. Example 1: computed squared synchronization error and the theorem's Mittag–Leffler upper bound for $\alpha = 0.98$, $K = 1.5$.

10.1.6. Temporal and spatial sensitivity

To avoid estimating a convergence order against a reference solution that is not sufficiently fine, Table 3 uses the self-convergence differences

$$D_h := \left(\left\|c_h(T) - c_{h/2}(T)\right\|_2^2 + \left\|d_h(T) - d_{h/2}(T)\right\|_2^2\right)^{1/2}, \qquad p_h := \log_2\left(\frac{D_h}{D_{h/2}}\right).$$

The finest step $h = 0.000625$ is only used to form the last difference and rate. The rates decrease toward the theoretical L1 order $2 - \alpha = 1.02$ for $\alpha = 0.98$, rather than displaying an artificially high order caused by a coarse reference. Table 4 shows rapid spectral convergence.

Table 3. Example 1: temporal self-convergence for $N = 8$, $\alpha = 0.98$, and $K = 1.5$.

h	$D_h = \|Y_h(T) - Y_{h/2}(T)\|_2$	p_h	Final sync. error
0.0400	1.8001×10^{-3}	1.151	4.7883×10^{-3}
0.0200	8.1070×10^{-4}	1.103	4.6379×10^{-3}
0.0100	3.7731×10^{-4}	1.077	4.5704×10^{-3}
0.0050	1.7883×10^{-4}	1.063	4.5386×10^{-3}
0.0025	8.5569×10^{-5}	1.056	4.5231×10^{-3}

Table 4. Example 1: spatial-mode sensitivity against the $N = 12$ reference solution ($h = 0.01$, $\alpha = 0.98$, $K = 1.5$).

N	Combined coefficient error	Final sync. error
4	5.0712×10^{-4}	4.5703×10^{-3}
6	2.4601×10^{-5}	4.5704×10^{-3}
8	3.9878×10^{-7}	4.5704×10^{-3}
10	1.7782×10^{-8}	4.5704×10^{-3}
12	reference	4.5704×10^{-3}

Conclusion of Example 1. This experiment directly validates the principal claims requested for the full PDE: the numerical solution is spatially distributed, both integral constraints are preserved to machine precision, the gain dependence agrees with the sufficient theorem threshold, orders below 0.9 are tested, the computed decay respects the Mittag–Leffler estimate, and the temporal and spatial refinements are stable. No Lorenz reduction is used in this first example.

10.2. Example 2: constraint-preserving chaotic invariant-modal benchmark

Having completed the direct validation of the local PDE in Example 1, we now turn to the auxiliary System (8.6)–(8.7). Its first three admissible spatial modes form the invariant saturated Lorenz-type Subsystem (8.9); the reconstructed field retains the constrained operator representation and satisfies both integral moments. Because the diffusion is compensated on these modes and all higher modes decay, the conclusions below concern chaotic invariant-modal dynamics and their synchronization, not high-dimensional spatiotemporal chaos.

10.2.1. Chaotic modal geometry and spatial reconstruction

Figures 8 and 9 use the drive trajectory after discarding the transient interval $0 \le t < 30$. The three modal coordinates form a persistent double-scroll set, while the reconstructed field

$$u_N(x,t) = \sum_{j=1}^{3} z_j(t)\phi_j(x) \tag{10.4}$$

shows irregular switching of spatial profiles. Thus, the chaotic signal is represented by a field that satisfies the same integral constraints and diffusion realization as the analytical problem.

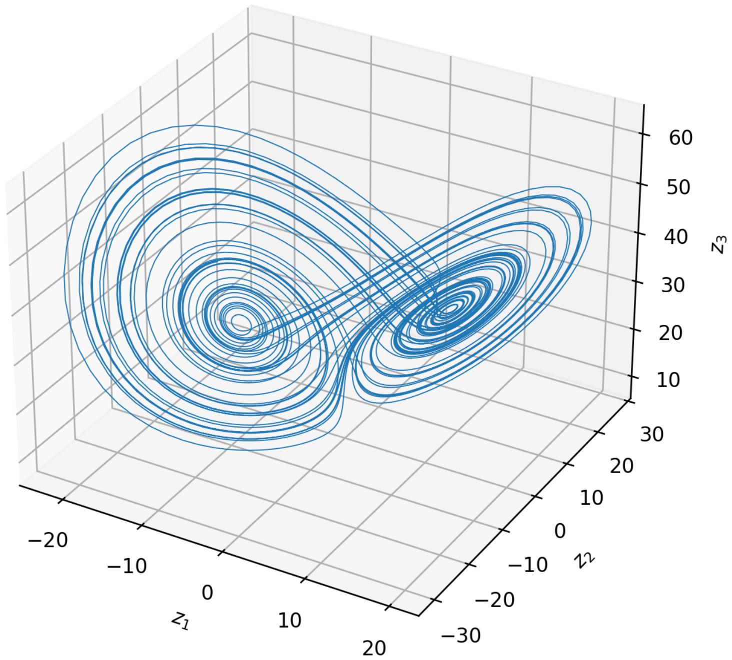

Figure 8. Example 2: double-scroll trajectory of the first three admissible PDE modes for $\alpha = 0.98$, $R = 50$, and $30 \leq t \leq 100$.

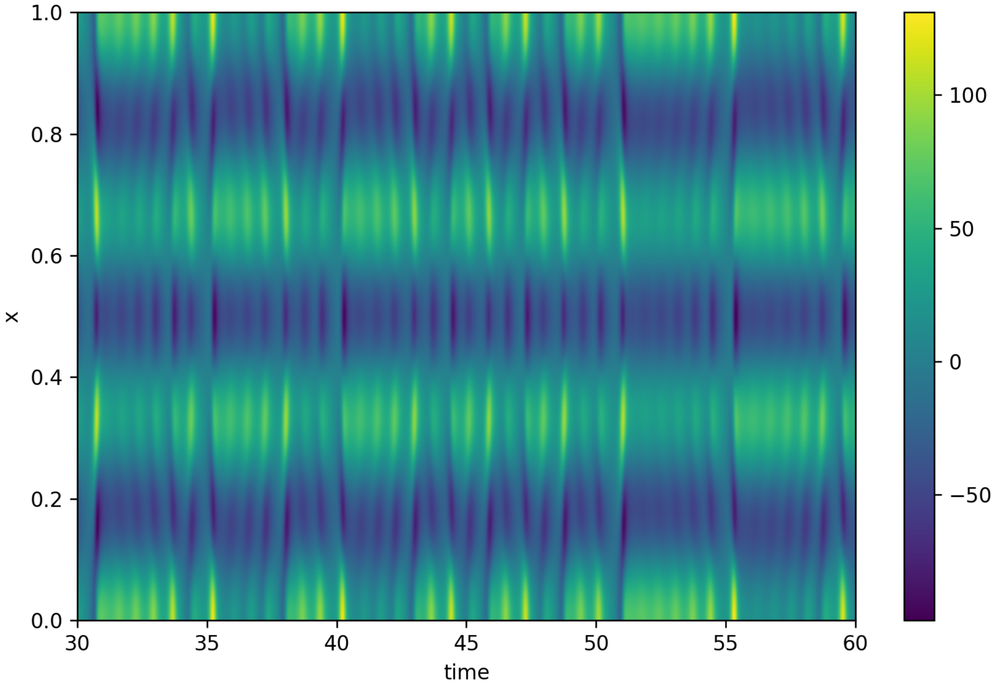

Figure 9. Example 2: spatial reconstruction of the chaotic invariant-modal benchmark on $30 \leq t \leq 60$. Both integral moments vanish for every displayed time.

10.2.2. Quantitative chaos diagnostics

For a quantitative diagnostic, the correlation implementation of the Gottwald–Melbourne 0–1 test [28] is applied to $z_1(t)$ after the transient. The signal is sampled every 0.1 time units to avoid the known oversampling bias, and the statistic is evaluated for 100 independently selected values of the test parameter. The median is

$$K_{01} = 0.992769, \tag{10.5}$$

with 10%, 50%, and 90% quantiles 0.868974, 0.992769, and 0.998478, respectively. Values near one indicate chaotic dynamics. Figure 10 shows that the distribution is strongly concentrated near one.

A second trajectory is started from $(1 + 10^{-8}, 1, 1)^\top$. Before the separation reaches the attractor scale, a least-squares fit of $\log \|z(t) - \widetilde{z}(t)\|_2$ gives the positive finite-time rate

$$\widehat{\lambda}_{\mathrm{FT}} = 0.927839. \tag{10.6}$$

This is reported as a finite-time sensitivity diagnostic, not as a rigorous asymptotic Lyapunov exponent. Its positivity, together with the 0–1 statistic and the double-scroll geometry, provides mutually consistent numerical evidence for chaos.

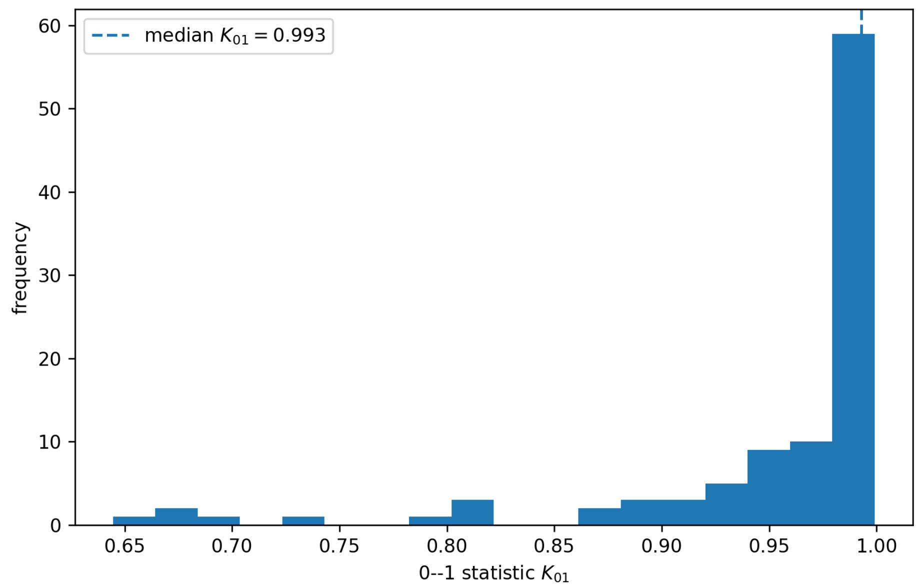

Figure 10. Example 2: distribution of the 0–1 chaos statistic for 100 test parameters; the median value is $K_{01} = 0.993$.

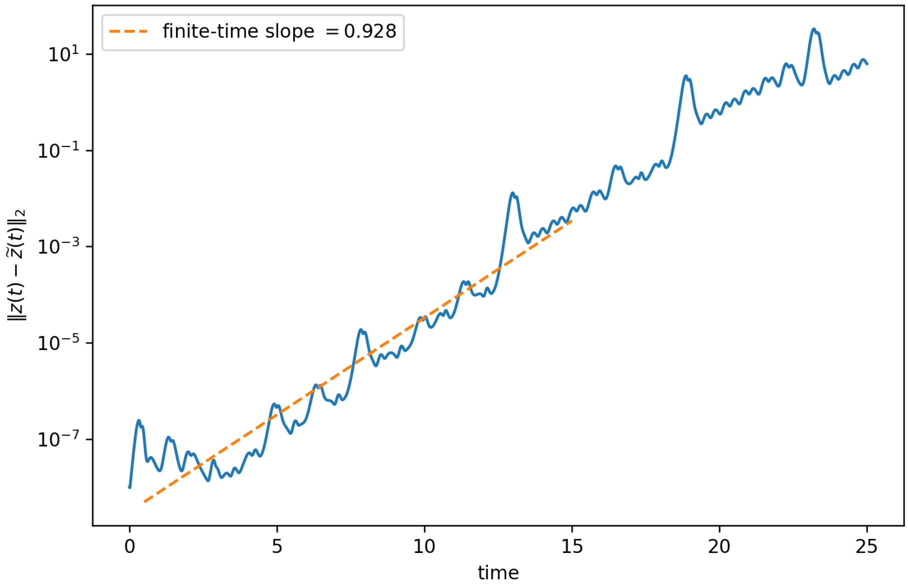

Figure 11. Example 2: growth of the separation between two chaotic PDE trajectories whose first modal coefficients initially differ by 10^{-8}.

10.2.3. Synchronization of two copies of the chaotic PDE

Finally, Figure 12 and Table 5 test synchronization of two copies of the same chaotic PDE. Without coupling, the error remains of the attractor size. At $K = 2$ and $K = 5$, the coefficient error is reduced to approximately 10^{-3} by $T = 40$, while all spatial moments remain at the roundoff level.

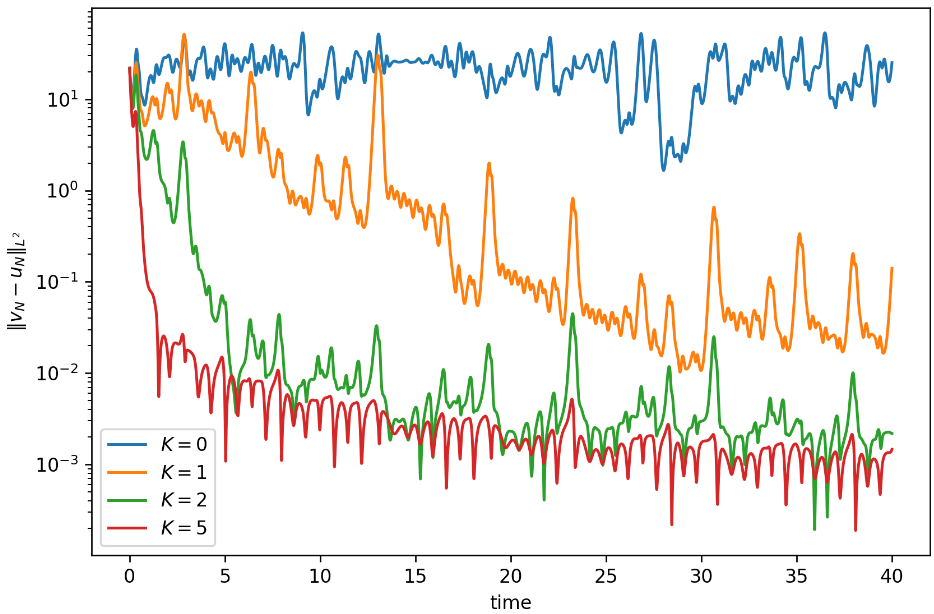

Figure 12. Example 2: synchronization error for the constrained chaotic PDE at $\alpha = 0.98$.

Table 5. Example 2: drive–response synchronization of the chaotic constrained PDE at $T = 40$.

K	Final error	Mean, last 100 steps	Maximum, last 100 steps
0	2.5067×10^{1}	1.9015×10^{1}	2.7512×10^{1}
1	1.4061×10^{-1}	3.2572×10^{-2}	1.4061×10^{-1}
2	2.1853×10^{-3}	2.0899×10^{-3}	2.4162×10^{-3}
5	1.4651×10^{-3}	1.1068×10^{-3}	1.4651×10^{-3}

Conclusion of Example 2. The double-scroll geometry, the near-unit 0–1 statistic, the positive finite-time separation rate, and the successful coupling of two copies provide consistent numerical evidence for chaotic dynamics on the three-mode invariant manifold. Therefore, Example 2 complements rather than replaces Example 1: the first validates the full reaction–diffusion PDE and the theorem, whereas the second tests compatibility of the constrained operator framework with chaotic modal dynamics. It is not used to claim high-dimensional spatiotemporal chaos.

11. Discussion

The analytical framework separates three mechanisms. First, the moment subspace and its projection provide a precise weak interpretation of the integral constraints. Second, the form-generated operator supplies the spatial dissipation and the fractional-resolvent smoothing needed to treat a gradient-dependent nonlinearity in $D(\mathcal{A}^{1/2})$. Third, the coupling gain directly contributes to the error dissipation.

Threshold (6.3) quantifies the derivative mismatch rather than hiding it in an unspecified constant. The term $L_1^2/(4\delta a_0)$ represents the cost of absorbing the gradient difference, while $(1 - \delta)a_0\pi^2$ is the remaining constrained diffusion. Optimizing over $\delta \in (0, 1)$ can sharpen the sufficient gain.

The numerical section tests the same operator and moment conditions as the theory. The local reaction–diffusion benchmark validates the analytical threshold, exact constraint enforcement, and numerical convergence. The second benchmark is explicitly limited to a three-mode invariant manifold. Its spatial reconstruction, double-scroll portrait, 0–1 statistic, and finite-time sensitivity give consistent evidence of chaotic modal dynamics, and the coupling experiment synchronizes two copies of this constrained modal benchmark. Because diffusion is compensated on the active modes and higher modes decay, these computations are not interpreted as high-dimensional spatiotemporal chaos.

12. Conclusions

We developed a rigorous framework for time-fractional drive–response reaction–diffusion systems under two integral moment constraints. The constrained spaces, projection, lifting, operator domain, coercivity, density, admissible trace space, fractional resolvent formulation, and energy space were explicitly specified. Global mild solutions were obtained on arbitrary finite intervals through a weighted fixed-point argument that respects the unbounded elliptic operator and the memory of the Caputo derivative. A spectral Galerkin convergence argument justifies the passage of the synchronization bound to energy-space mild solutions, and the resulting Mittag–Leffler theorem controls the spatial-derivative mismatch explicitly. The full reaction–diffusion discretization verified the moment conservation, gain dependence, fractional orders below 0.9, corrected temporal self-convergence approaching $2 - \alpha$, spatial convergence, and the theoretical decay bound. The auxiliary three-mode benchmark exhibited a double-scroll trajectory, a median 0–1 statistic of 0.993, positive finite-time separation, and successful synchronization on its invariant modal manifold. This last experiment demonstrates compatibility with chaotic modal dynamics but is not claimed to establish high-dimensional spatiotemporal chaos.

Future work may address noncommensurate orders, state-dependent or adaptive gains, higher-dimensional moment manifolds, stochastic forcing, and rigorous error estimates for the nonlinear spectral–L1 discretization.

Author contributions

A. Menasri: Conceptualization, Methodology, Formal analysis, Software, Numerical investigation, Visualization, Writing–original draft; A. Merad: Supervision, Validation, Writing–review and editing. Both authors have read and approved the final version of the manuscript.

Use of Generative-AI tools declaration

The authors used ChatGPT (OpenAI) solely to assist with English-language proofreading and editorial refinement during the final proof stage. The authors reviewed and approved all changes and take full responsibility for the content of the article.

Acknowledgments

The authors sincerely thank the anonymous reviewers for their valuable comments and constructive assessment, which helped improve the quality of the manuscript. The authors also express their gratitude to the Editor and the Editorial Office of *AIMS Mathematics* for their professional handling, support, and assistance throughout the review and publication process.

Conflict of interest

A. Merad is the Guest Editor of the Special Issue ”Advances in Differential Equations: Methods and Applications” for AIMS Mathematics. A. Merad was not involved in the editorial review and the decision to publish this article. The authors declare that they have no conflicts of interest.

References

1. I. Podlubny, *Fractional differential equations*, San Diego: Academic Press, 1999.
2. K. Diethelm, *The analysis of fractional differential equations*, Berlin: Springer, 2010. http://doi.org/10.1007/978-3-642-14574-2
3. A. A. Kilbas, H. M. Srivastava, J. J. Trujillo, *Theory and applications of fractional differential equations*, Amsterdam: Elsevier, 2006.

4. Y. Zhou, *Basic theory of fractional differential equations*, Singapore: World Scientific, 2014. http://doi.org/10.1142/9069

5. K. Sakamoto, M. Yamamoto, Initial value/boundary value problems for fractional diffusion-wave equations and applications to some inverse problems, *J. Math. Anal. Appl.*, **382** (2011), 426–447. http://doi.org/10.1016/j.jmaa.2011.04.058

6. R.-N. Wang, D.-H. Chen, T.-J. Xiao, Abstract fractional Cauchy problems with almost sectorial operators, *J. Differ. Equations*, **252** (2012), 202–235. http://doi.org/10.1016/j.jde.2011.08.048

7. R. Zacher, A De Giorgi–Nash type theorem for time-fractional diffusion equations, *Math. Ann.*, **356** (2013), 99–146. http://doi.org/10.1007/s00208-012-0834-9

8. A. Al-Khateeb, H. Zureigat, K. Abuasbeh, E. Fadhal, Leray–Schauder alternative for the existence of solutions of a modified coupled system of Caputo fractional differential equations with two-point integral boundary conditions, *Symmetry*, **15** (2023), 863. http://doi.org/10.3390/sym15040863

9. Z. Cui, Z. Zhou, Existence of solutions for Caputo fractional delay differential equations with nonlocal and integral boundary conditions, *Fixed Point Theory Algorithms Sci. Eng.*, **2023** (2023), 1. http://doi.org/10.1186/s13663-022-00738-3

10. E. Alhazzani, S. Mesloub, H. E. Gadain, On the solvability of a singular time fractional parabolic equation with nonclassical boundary conditions, *Fractal Fract.*, **8** (2024), 189. http://doi.org/10.3390/fractalfract8040189

11. S. Mesloub, E. Alhazzani, H. E. Gadain, A two-dimensional nonlocal fractional parabolic initial boundary value problem, *Axioms*, **13** (2024), 646. http://doi.org/10.3390/axioms13090646

12. K. M. Owolabi, B. Karaagac, Chaotic and spatiotemporal oscillations in fractional reaction-diffusion system, *Chaos Soliton. Fract.*, **141** (2020), 110302. http://doi.org/10.1016/j.chaos.2020.110302

13. K. M. Owolabi, Numerical approach to chaotic pattern formation in diffusive predator–prey system with Caputo fractional operator, *Numer. Meth. Part. Differ. Equ.*, **37** (2021), 131–151. http://doi.org/10.1002/num.22522

14. C. Tan, T. Lei, M. Zou, Y. Liang, L. Chen, P. Tang, et al., Manipulating circular Airy beam dynamics with quadratic phase modulation in fractional systems under some diffraction modulations and potentials, *Opt. Express*, **32** (2024), 25261–25275. http://doi.org/10.1364/OE.528156

15. C. Tan, Y. Liang, M. Zou, M. Liu, L. Zhang, Controllable trajectory Hermite–Gaussian vortex beams in nonlinear fractional Schrödinger systems, *Chaos Soliton. Fract.*, **194** (2025), 116261. http://doi.org/10.1016/j.chaos.2025.116261

16. M. Khan, A. Rasheed, M. S. Anwar, Numerical analysis of nonlinear time-fractional fluid models for simulating heat transport processes in porous medium, *ZAMM Z. Angew. Math. Mech.*, **103** (2023), e202200544. http://doi.org/10.1002/zamm.202200544

17. M. Khan, A. Rasheed, The space–time coupled fractional Cattaneo–Friedrich Maxwell model with Caputo derivatives, *Int. J. Appl. Comput. Math.*, **7** (2021), 112. http://doi.org/10.1007/s40819-021-01027-0

18. M. Khan, A. Alhowaity, M. Imran, M. Hussien, R. Alroobaea, M. S. Anwar, Advanced numerical simulation techniques in MHD fluid flow analysis using distributed fractional order derivatives and Cattaneo heat flux model, *ZAMM Z. Angew. Math. Mech.*, **104** (2024), e202300622. http://doi.org/10.1002/zamm.202300622
19. M. Khan, M. S. Anwar, Distributed-order time-fractional analysis of non-Newtonian Sisko fluid flow under magneto-thermal effects, *Propuls. Power Res.*, **14** (2025), 707–722. http://doi.org/10.1016/j.jppr.2025.12.001
20. M. Khan, A. Rasheed, Numerical implementation and error analysis of nonlinear coupled fractional viscoelastic fluid model with variable heat flux, *Ain Shams Eng. J.*, **13** (2022), 101614. http://doi.org/10.1016/j.asej.2021.10.009
21. K. Diethelm, N. J. Ford, A. D. Freed, A predictor–corrector approach for the numerical solution of fractional differential equations, *Nonlinear Dyn.*, **29** (2002), 3–22. http://doi.org/10.1023/A:1016592219341
22. M. Zheng, F. Liu, I. Turner, V. Anh, A novel high order space–time spectral method for the time fractional Fokker–Planck equation, *SIAM J. Sci. Comput.*, **37** (2015), A701–A724. http://doi.org/10.1137/140980545
23. D. Liu, T. Li, X. He, Fixed-time multi-switch combined–combined synchronization of fractional-order chaotic systems with uncertainties and external disturbances, *Fractal Fract.*, **7** (2023), 281. http://doi.org/10.3390/fractalfract7040281
24. C. Zhang, Y. Gao, J. Yao, F. Qian, Synchronization of bidirectionally coupled fractional-order chaotic systems with unknown time-varying parameter disturbance in different dimensions, *Mathematics*, **12** (2024), 2775. http://doi.org/10.3390/math12172775
25. T. Hamadneh, A. Hioual, R. Saadeh, M. A. Abdoon, D. K. Almutairi, T. A. Khalid, et al., General methods to synchronize fractional discrete reaction–diffusion systems applied to the glycolysis model, *Fractal Fract.*, **7** (2023), 828. http://doi.org/10.3390/fractalfract7110828
26. C. Yang, J. Wang, M. Jian, J. Dai, Synchronization control of complex spatio-temporal networks based on fractional-order hyperbolic PDEs with delayed coupling and space-varying coefficients, *Fractal Fract.*, **8** (2024), 525. http://doi.org/10.3390/fractalfract8090525
27. R. Zhang, K. Qiu, C. Liu, H. Ma, Z. Chu, Comparison-principle-based synchronization analysis of fractional-order chaotic neural networks with multi-order and its circuit implementation, *Fractal Fract.*, **9** (2025), 273. http://doi.org/10.3390/fractalfract9050273
28. G. A. Gottwald, I. Melbourne, On the implementation of the 0–1 test for chaos, *SIAM J. Appl. Dyn. Syst.*, **8** (2009), 129–145. http://doi.org/10.1137/080718851

AIMS Press

© 2026 Menasri and Merad, licensee AIMS Press. This is an open access article distributed under the terms of the Creative Commons Attribution License (https://creativecommons.org/licenses/by/4.0)